A 2000-volumes/s 3-D Ultrasound Probe With Monolithically-Integrated 23 × 23-mm² 4096 -Element CMUT Array

Rozsa, Nuriel N.M.; Kim, Taehoon; Guo, Peng; Hopf, Yannick M.; Dos Santos, Djalma Simoes; Noothout, Emile; Chang, Zu Yao; Chen, Chao; De Jong, Nico; Vos, Hendrik J.

DOI
10.1109/JSSC.2025.3534087

Publication date
2025

Document Version
Final published version

Published in
IEEE Journal of Solid-State Circuits

A 2000-volumes/s 3-D Ultrasound Probe With Monolithically-Integrated 23 × 23-mm^2 4096-Element CMUT Array

Nuriel N. M. Rozsa, *Member, IEEE*, Zhao Chen, *Member, IEEE*, Taehoon Kim, *Member, IEEE*, Peng Guo, *Member, IEEE*, Yannick M. Hopf, *Member, IEEE*, Jason Voorneveld, *Member, IEEE*, Djalma Simoes dos Santos, *Member, IEEE*, Emile Noothout, Zu-Yao Chang, Chao Chen, *Member, IEEE*, Vincent A. Henneken, Nico de Jong, *Member, IEEE*, Hendrik J. Vos, *Member, IEEE*, Johan G. Bosch, *Member, IEEE*, Martin D. Verweij, *Member, IEEE*, and Michiel A. P. Pertijs, *Senior Member, IEEE*

***Abstract*— This article presents a 4096-element ultrasound probe for high volume-rate (HVR) cardiovascular imaging. The probe consists of two application-specific integrated circuits (ASICs), each of which interfaces with a 2048-element monolithically-integrated capacitive micro-machined ultrasound transducer (CMUT) array. The probe can image a 60° × 60° × 10-cm volume at 2000 volumes/s, the highest volume-rate with in-probe channel-count reduction reported to date. It uses 2 × 2 delay-and-sum micro-beamforming (μBF) and 2× time-division multiplexing (TDM) to achieve an 8× receive (RX) channel-count reduction. Equalization, trained using a pseudorandom bit-sequence generated on the chip, reduces TDM-induced crosstalk by 10 dB, enabling power-efficient scaling of the cable drivers. The ASICs also implement a novel transmit (TX) beamformer (BF) that operates as a programmable digital pipeline, which enables steering of arbitrary pulse-density modulated (PDM) waveforms. The TX BF drives element-level 65 V unipolar pulsers, which in turn drive the CMUT array. Both the TX BF and RX μBF are programmed with shift-registers (SRs) that can either be programmed in a row-column fashion for fast upload times, or daisy-chain fashion for a higher flexibility. The layout of the ASICs is matched to the 365-μm-pitch monolithically-integrated CMUT array. While operating, the RX and logic power consumption per element is 0.85 and 0.10 mW, respectively. TX power consumption is highly waveform dependent, but is nominally 0.34 mW. Compared to the prior art, the probe has the highest volume rate, and features among the largest imaging arrays (both in terms of element-count and aperture) with a high flexibility in defining the TX waveform. These properties make it a suitable option for applications requiring HVR imaging of a large region of interest.**

***Index Terms*— 3-D, abdominal aortic aneurysms (AAAs), application-specific integrated circuit (ASIC), B-mode, beamformer (BF), beamforming, capacitive micro-machined ultrasound transducer (CMUT), cardiovascular, equalization, high volume-rate (HVR), pseudorandom bit sequence (PRBS), time-division multiplexing (TDM), ultrasound imaging.**

Received 23 August 2024; revised 11 December 2024; accepted 13 January 2025. Date of publication 11 February 2025; date of current version 28 March 2025. This article was approved by Associate Editor Ron Kapusta. This work was supported in part by the Ultra-X-Treme Project through Netherlands Organization for Scientific Research under Grant P17-32. *(Corresponding author: Nuriel N. M. Rozsa.)*

Nuriel N. M. Rozsa, Taehoon Kim, Peng Guo, Zu-Yao Chang, and Michiel A. P. Pertijs are with the Department of Microelectronics, Delft University of Technology, 2628 CM Delft, The Netherlands (e-mail: n.n.m.rozsa@tudelft.nl).

Zhao Chen and Vincent A. Henneken are with Philips Innovation and Strategy, 5656 AE Eindhoven, The Netherlands.

Yannick M. Hopf is with the Department of Microelectronics, Delft University of Technology, 2628 CM Delft, The Netherlands, and also with Sonosilicon, 2629 JD Delft, The Netherlands.

Jason Voorneveld and Johan G. Bosch are with the Department of Cardiology, Thorax Biomedical Engineering, Erasmus MC University Medical Center, 3015 GD Rotterdam, The Netherlands.

Djalma Simoes dos Santos and Emile Noothout are with the Department of Imaging Physics, Delft University of Technology, 2628 CJ Delft, The Netherlands.

Chao Chen is with the Department of Microelectronics, Delft University of Technology, 2628 CM Delft, The Netherlands, and also with Sonosilicon, Hangzhou, Zhejiang 310059, China.

Nico de Jong, Hendrik J. Vos, and Martin D. Verweij are with the Department of Imaging Physics, Delft University of Technology, 2628 CJ Delft, The Netherlands, and also with the Department of Cardiology, Thorax Biomedical Engineering, Erasmus MC University Medical Center, 3015 GD Rotterdam, The Netherlands.

Color versions of one or more figures in this article are available at https://doi.org/10.1109/JSSC.2025.3534087.

Digital Object Identifier 10.1109/JSSC.2025.3534087

I. Introduction

ABDOMINAL aortic aneurysm (AAA) ruptures are a common cause of sudden death [1]. Patients at risk of AAA rupture have an abdominal aorta (AA) with a diameter exceeding 5.5 cm for men or 5.0 cm for women, and/or a yearly increase of more than 1.0 cm [2]. In clinical practice, the risk of AAA rupture is assessed using geometrical data, acquired from multiple 2-D cross-sectional images using a 1-D ultrasound transducer array [3]. This method of diagnosis is commonly used, as it is safe and noninvasive [3], [4]. Its working principle involves transmit (TX) ultrasound beams and receive (RX) their reflections. Images are then reconstructed from the time-of-flight and magnitude of the RX signals, the former mapping object locations and the latter determining contrast.

However, accurate AAA diagnosis requires more data than the AA diameter, such as elasticity and blood flow. This data is ideally gathered in 3-D, rather than with one or multiple cross-sectional scans [3], [4], [5], [6], [7], [8]. Accordingly, modern imaging techniques such as 3-D flow and 3-D elastography are investigated. These techniques require 3-D imaging probes with 2-D transducer arrays, consisting of thousands of elements, capable of reconstructing volumes at kilohertz rates [4], [5], [9].

Commercial probes that use direct-element connections are constrained to arrays of roughly 1000 elements [7], [9] due to interconnect limitations [4]. Using such probes implies sharp compromises in image contrast [10], resolution [4], and/or penetration depth, limiting their applicability. Probes with large imaging arrays that use row-column addressing have a limited field-of-view (FoV) [11], making them unsuitable for this application. Probes with large array sizes and with a sufficiently large FoV require channel-count reduction techniques [4], for which in-probe application-specific integrated circuits (ASICs) are well suited.

Broadly, channel-count reduction techniques can be divided into two categories: techniques that reduce channel count at the cost of a reduction in volume rate, and techniques that exploit RX signal characteristics to reduce channel count without reducing volume rate. The first category includes techniques such as micro-beamforming (μBF) [12], [13], [14], [15], [16], [17], element summation [18], and/or synthetic aperture imaging [17], [18], [19], [20]. As each of these techniques requires multiple TX/RX acquisitions to reconstruct a volume, they can only be applied for high volume-rate (HVR) imaging to a limited extent. With μBF [12], [13], [14], [15], [16], [17], the transducer array is divided into multiple sub-arrays, in which the RX signals per element are combined into a single channel by a delay-and-sum operation. This operation yields a preprogrammed directivity of the sub-array, i.e., only a smaller sub-volume is scanned with one single T/R acquisition. Therefore, scanning the full FoV requires multiple T/R acquisitions, which are combined to reconstruct the full volume. Element summation, i.e., summing without delaying [18], can be seen as a simplification of μBF, where the sub-arrays can only be "forward" looking. As a result, the volume that can be imaged compared to μBF is reduced. Synthetic aperture imaging [17], [18], [19], [20] is a multiplexing (MUX) technique, in which only a subset of elements is selected during TX and/or RX per acquisition, and all signals are combined in the later volume reconstruction step. However, multiple acquisitions are required to obtain a full volumetric dataset, reducing the volume rate. Moreover, since the recorded sub-volumes are captured sequentially, any motion in between the capturing leads to reconstruction artifacts [21], [22].

Techniques in the second category, which reduce channel count without sacrificing volume rate, include analog time-division MUX (TDM) [15], [23], [24], [25], frequency-division MUX (FDM) [26], or digital TDM (D-TDM) [14], [18]. These techniques exploit the limited bandwidth of element-level RX signals by modulating multiple signals onto a higher-bandwidth output channel. However, this introduces crosstalk (for TDM and FDM) or bit-errors (for D-TDM), leading to imaging artifacts. Moreover, these techniques are limited by the bandwidth of the cable that connects the probe to an imaging system, or by that of the system RX channel [27], [28]. As a result, practical ultrasound systems can only make limited use of these techniques.

Currently reported probes with ASICs also have constrained TX waveform programmability, resulting from limitations in their counter-based TX beamformer (TX BF) architecture [14], [17], [29], [30], on-chip pulsers [18], [31] and/or signal distribution network [31]. The extent of this limitation varies per design. For instance, some designs can TX an arbitrary pulse train, with a semi-fixed duty cycle [14], [29]. The design in [31] provides more pulse shape programmability, but the waveform length and BF delays are restricted. These restrictions have been reduced with a BF that propagates a more freely programmable TX waveform across its array [18]. Nevertheless, no design has made both the pulse shape and length arbitrary to the same extent as probes with direct-element connections, trading off flexibility in TX waveform generation with system complexity, often precluding applications requiring more complex waveforms than simple pulses or pulse trains [32], [33].

This article presents a novel 3-D probe design, targeting cardiovascular imaging applications requiring HVR and LVI, such as AAA functional imaging. This application requires imaging of a 60° × 60° × 10-cm volume at 2000 volumes/s, which is sufficient to image the flow and wall motion of the AA, and is the highest volume-rate for designs with in-probe channel-count reduction reported to date. The full probe consists of two tiled ASICs, each monolithically integrated with a 32 × 64-element array of capacitive micromachined ultrasound transducers (CMUTs) with a 2.6-MHz center frequency. Each ASIC provides 8× channel-count reduction by means of 2 × 2 delay-and-sum μBFs and 2× TDM, thus exploiting the benefits of both techniques without reducing the frame rate below the acceptable limit (2000 volumes/s) or straining the requirements for the back-end RX system—thus, the probe can interface with two commonly-used Verasonics Vantage-256 (VSX) imaging systems [4], [7], [27]. The μBF architecture in the ASIC is based on the design in [30], but provides an 80% larger delay range to image the specified FoV. TDM-induced crosstalk from channel-bandwidth limitations is mitigated with equalizers (EQs), consisting of finite-impulse-response (FIR) filters that the system trains with a pseudorandom bit sequence (PRBS) generated on chip. By calibrating the frequency response of each channel, the on-chip cable driver bandwidth can be reduced, in turn making the system more power efficient.

The probe also contains a novel TX BF that provides a high degree of flexibility in TX waveform definition, while having a relatively low system complexity. It steers arbitrary pulse-density modulated (PDM) waveforms to two-level 65-V unipolar pulsers, driving each element. Similar to the TX BF presented in [18], waves are propagated across the array by means of programmable delay cells, integrated per element. However, the presented probe does so in a row-column fashion, rather than with a delay mesh. This simplifies the per-element TX BF logic, while maintaining the ability to define arbitrary BF delays.

This article is structured as follows. Section II covers the design requirements for the intended application and the associated system architecture. Section III covers the circuit design of the ASICs and Section IV covers their integration with CMUTs and packaging. Section V presents the characterization and imaging results of fabricated prototypes. The article ends with Section VI, which contains a comparison to prior designs and a conclusion.

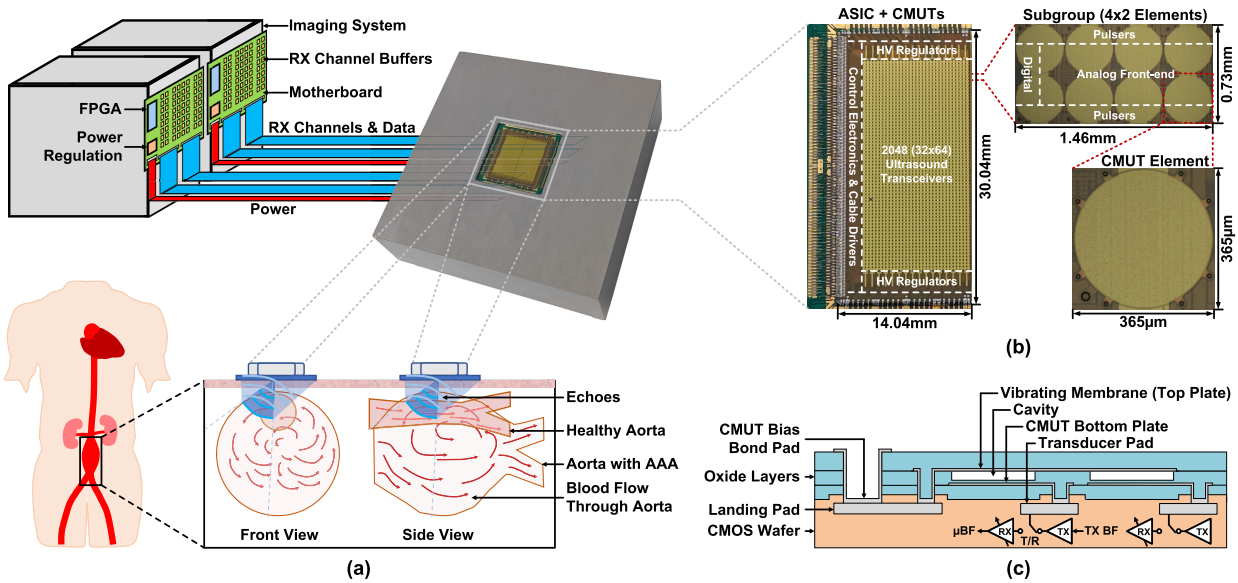

Fig. 1. (a) Overview of the developed system and its application. (b) Overview of an ASIC + CMUTs and a breakdown of the replicated modules. (c) Simplified cross section of the CMUT design.

II. System Design

A. Application and System Overview

Fig. 1(a) shows an overview of the developed system and its application. It consists of the imaging probe with ASICs plus CMUTs, the aperture of which is divisible in two halves (tiles) that can independently interface with a system back-end. This consists of two duplicate motherboards and imaging systems. Each motherboard buffers the RX channels from one tile, regulates its various supplies, and contains an FPGA to configure the probe. The imaging systems digitize the RX signals and do image reconstruction.

Although the main targeted application is imaging of the AA, the features of the probe are equally applicable in other parts of the cardiovascular system, such as the heart [34]. The probe's packaging was designed to be compatible with various research setups by having a flat waterproof front-side and various mounting points at the back of the casing. This packaging is covered in more detail in Section IV.

Fig. 1(b) shows an overview of one tile. It consists of two independent 32 × 32-element halves that are subdivided into 4 × 2-element subgroups reducing the echo signals received by the eight subgroup elements to one output RX channel. These are routed to the periphery of the chip, where they are buffered and connected to the off-chip system back-end.

Fig. 1(c) shows the simplified monolithically-integrated CMUT layer stack. The CMUTs are Philips 365-μm-pitch CM5 devices [35], [36] and have been fabricated on an ASIC that is made with a TSMC 0.18-μm BCD process. This process provides both high-voltage (HV) double-diffused metal-oxide-semiconductor (DMOS) and low-voltage (LV) complementary metal-oxide semiconductor (CMOS) devices, the former being required for the on-chip TX circuits and the latter for the RX circuits and logic. Each CMUT connects to a TX and RX front end, which are separated by a T/R switch. Although the probe presented in this work contains CMUTs, both the RX and TX front-ends have been designed to also be compatible with bulk-piezo transducers (PZT), similar to those used in [17] and [30], but at a lower frequency.

B. Architecture

Fig. 2 shows the system architecture implemented in the presented design. Because each tile is subdivided in independent ASIC halves, the full probe consists of independently operable quarters. Each ASIC half contains periphery circuitry and a core that consists of an array of subgroups. The system clock (CLK_{SYST}) operates at a frequency (f_{SYST}) of 31.25 MHz, which defines a time resolution (T_{SYST}) for both the TX BF and μBF of 32 ns.

The probe targets a 10-cm imaging depth. Given the speed of sound in human tissue, the resulting maximum pulse-repetition frequency (PRF) is 7.7 kHz. To achieve the targeted volume-rate of ~2000 volumes/s, the full volume of 60° × 60° × 10 cm needs to be reconstructed from at most four T/R acquisitions. As a result, to accommodate the μBF restrictions (covered later in this section) and to maximize the probe's round-trip dynamic range (DR), the four targeted TX beams diverge 30° in both azimuth and elevation directions. However, in order to freely configure the probe for other imaging modes, narrower angles in both azimuth and/or elevation may be desired. Therefore, the probe is capable of freely configuring its delay profile for each T/R cycle.

Fig. 3(a) shows the TX BF architecture. It contains a column and row section, each consisting of an array of delay cells. The column section is located at the ASIC periphery. By means of an input-selection multiplexer, each cell can either take the external PDM-modulated input TX_{IN} (indicated with "E" on the multiplexer), or take its input from a neighboring cell (indicated with vertical arrows on the multiplexer). This allows the signal to propagate vertically and be passed to the row sections. Similarly, the cells in each row take either the output of the corresponding column cell or of a neighbor, as indicated with the "R" and the horizontal arrows, respectively, in the row-cell input-selection mux, propagating

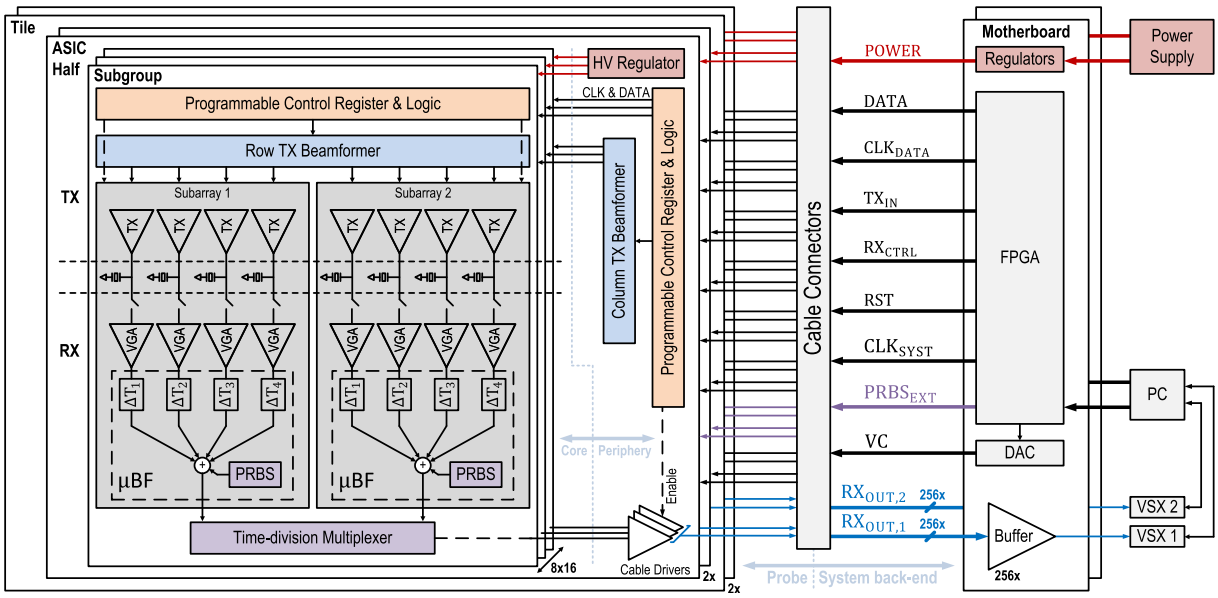

Fig. 2. Overview of the developed system architecture.

the signal horizontally. Both row and column cells implement a delay range of 0–7 clock periods (delays are indicated with the δ-blocks). This provides a cumulative delay range of $7 \times (64+64) \times T_{SYST} \approx 28.7\ \mu s$ across the array, as needed to implement the maximum delay difference between elements in the array. Because the TX BF only delays TX_{IN}, the waveform can have an arbitrary shape and length.

The TX BF is programmed with a shift-register (SR) that is controlled by an external data and a clock signal. As shown in Fig. 3(b), the TX BF can be programmed in a row-column fashion for optimal speed, or in a daisy-chain fashion for optimal flexibility. Fig. 3(c) provides a few example delay profiles and their corresponding programmed settings with this TX BF. As indicated, the arbitrary sum of delays in both columns and rows provides a wide range of waveforms that can be generated. Implementation details of the TX BF are discussed in Section III-A.

In TX, CMUTs are driven element-level with a two-level unipolar pulser. Although the pulser is capable of producing pulses with amplitudes between 5 and 65 V, the TX voltage is limited to 40 V. This ensures that the CMUTs remain in collapse mode and operate reliably when biased at +120 V at their ac ground [36]. The HV regulator at the ASIC periphery provides an additional supply for the pulser, which will be covered in Section III-B.

For RX, each CMUT connects to a low-noise variable-gain amplifier (VGA). As ultrasound waves exponentially attenuate with distance in human tissue, the round-trip DR per T/R cycle can be in the order of 100 dB [14], [29]. However, signal-to-noise ratio (SNR) requirements are typically only 40 dB. Therefore, the RX front-end implements time-gain-compensation (TGC) to decouple the system's SNR from its DR, resulting in an improved average power dissipation. The VGA has a continuous-gain range of 36 dB, which is controlled by an external analog signal (VC).

Each 4 × 2-element subgroup is divided into two 2 × 2-element subarrays, the echo signals of which are combined using a μBF with a programmable delay between 0 and

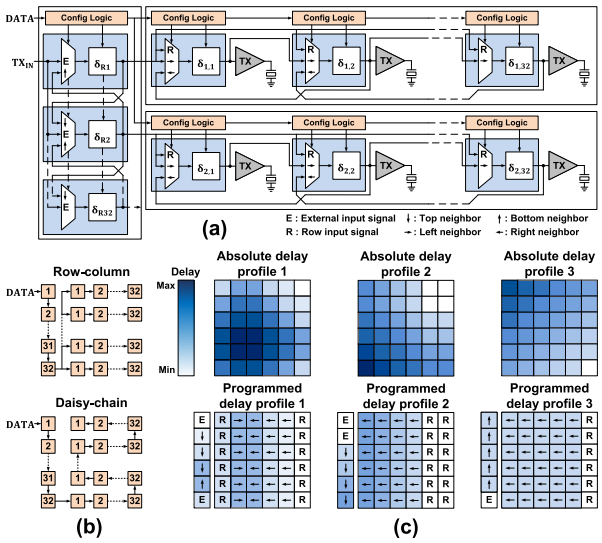

Fig. 3. (a) TX BF architecture. (b) Overview of programming configuration modes. (c) Example delay profiles and programmed settings for a simplified 6 × 6 array. Profile 1 is an angled focused beam, profile 2 is an angled diverging beam, and profile 3 is an angled plane wave.

8 clock periods. As a result of the summing operation involved with μBF, the FoV of each CMUT subarray reduces to 30°, thus requiring two viewing angles to cover a 60° FoV and four for a 60° × 60° FoV. As mentioned, the required 60° × 60° × 10 cm imaging volume is reconstructed from 4 T/R acquisitions using TX waveforms that cover a 30° × 30° FoV, one for each quadrant. Therefore, the directivity of the μBFs can be configured such that the FoV in RX matches TX. Both the VGA and μBF are based on the design in [30], but the μBF in this design has an 80% larger delay range to enable proper matching of the TX and RX FoV.

TDM is realized by having one of two μBFs periodically provide its output to a cable driver at the ASIC periphery. To minimize the load of the cable drivers, each RX channel is buffered at the system back-end before entering a VSX system. The VSX systems digitize and equalize all RX channels to compensate bandwidth limitations of the cable drivers.

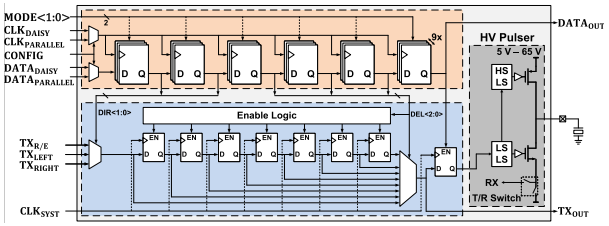

Fig. 4. Implementation of the element-level TX BF and pulser. DEL⟨2:0⟩ configures the signal delay, DIR⟨1:0⟩ configures the signal propagation direction and 1 bit enables the element HV pulser.

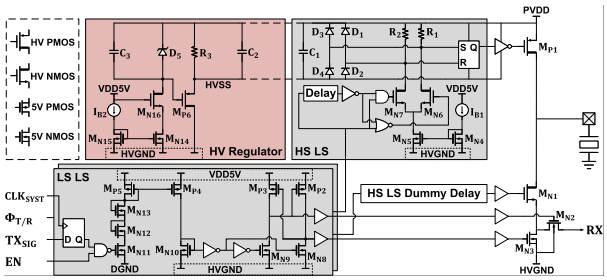

Fig. 5. Implementation of the element-level pulser and HV regulator at the ASIC periphery.

This reduces their bandwidth requirements, allowing for more power-efficient scaling. The EQs are trained with an on-chip generated PRBS, covered in more detail in Section V. Similar to the TX BF, the RX circuits can also be programmed in a row-column or daisy-chain fashion with a separate external data and clock signal.

III. Circuit Design

A. TX Beamformer

As indicated in Fig. 3, the TX BF consists of element-level delay cells that provide a delay difference between elements before transmitting TX_{IN}. Fig. 4 shows their implementation. As TX_{IN} is a PDM waveform that is sampled by CLK_{SYST}, it can be represented by a clocked binary sequence. Therefore, its delays can be implemented by a cascade of D-flip-flops (DFFs). To configure the per-element delays, the output of one of the cascaded DFFs is selected to be passed-on to the low-side level-shifters (LS LSs) of the HV pulser, and neighboring delay cells (TX_{OUT}). The DFFs that are not used per delay cell are disabled to reduce switching losses.

The following 6 bits are used to configure each delay cell: a 3-bit delay code (DEL) for selecting the output of the delay DFF, a 2-bit select code (DIR) for selecting the input propagation direction, and a 1-bit enable for the element HV pulser. To allow for fast switching between delay profiles, each cell contains 9 × 6 configuration DFFs, providing space for nine preloaded profiles. Their upload settings are configured with three external control signals. The CONFIG signal controls the data upload fashion [see Fig. 3(b)]. The MODE⟨1:0⟩ signal controls whether 1 or 9 profiles should be uploaded and whether the register should RX external data or loop previously uploaded local TX BF profile data per rising-edge of its input clock.

Each ASIC half contains one external data and a clock signal for the TX BF registers (see Fig. 2), but they are split into two signals at the periphery. This allows them to be routed together for both upload modes, guaranteeing them to be in-phase for each delay cell, preventing possible bit errors.

B. TX Pulser

Fig. 5 shows the element-level pulser design. The unipolar pulser driver stage, consisting of M_{P1}, M_{N1}, M_{N2}, and M_{N3}, is the same as the design in [29] and [37], but with an improved guard-ring design for prevention of latch-up. The DMOS transistors M_{P1} and M_{N1} switch the output voltage level, whereas M_{N2} and M_{N3} implement the T/R switch, connecting the CMUT to the VGA through M_{N1} and M_{N2} during RX, while isolating it from HV pulsing during TX. M_{P1} was scaled for driving strength, M_{N1} was scaled for driving strength and noise, M_{N2} was scaled for noise, and M_{N3} was scaled to minimize voltage ripple at the source of M_{N1}.

Two LS LS [38] stages convert the digital supply domain (DVDD-DGND) input signals to the 5-V domain (VDD5V-HVGND) and drive the T/R switch, high-side level-shifter (HS LS) and M_{N1}. Due to the large trace inductances from the long supply routing across the array, the high-side (PVDD-HVSS), power (PVDD-HVGND), and 5-V domains can experience significant ripple when in TX mode. Therefore, the diode-connected M_{N12} and M_{N13} are added to limit the voltage swing over M_{N11} and M_{P5}. The LS LS output is a latch that implements a break-before-make function to ensure that M_{P1}/M_{N1} and M_{N2}/M_{N3} are not on at the same time. The HS LS propagation delay is compensated with a dummy delay before the driver of M_{N1}.

The HS LS is based on the design in [39]. Its output is defined by an HS latch that operates in hold mode when both set and reset are "1" or "0," providing a high robustness against supply ripple. The latch is set or reset by means of pulsed inputs, generated through the IR drop across resistors R_1 and R_2 and the current drawn by an LS current-mirror, which is steered through DMOS transistors M_{N6} and M_{N7}. The pulsewidth is derived from a delay cell with a delay larger than the propagation delay of the TX signal through the HS LS and the HV pulser to ensure that the state of the HS latch does not change while the supply is most active.

The HS LS is powered by the pulser supplies PVDD and HVGND. PVDD can be varied between 5 and 65 V. The HVSS voltage, generated by an HV regulator at the ASIC periphery, is PVDD—5 V. The regulator is the same as in [29] and [37], while clamping diodes D_{1-4} are added per HS LS. These diodes ensure that the HS latch set and reset node voltages are kept between PVDD and HVSS ± diode voltage V_D. They also ensure that HVSS does not increase by more than V_D while the set or reset nodes are pulled down. This ensures reliable operation of the HS LS while transmitting longer pulse sequences, as the local supply capacitor C_1 can be recharged without transient currents from the regulator at the periphery, thus avoiding excessive voltage ripple at HVSS.

C. Variable-Gain Amplifier

The VGA is based on the design in [30] and [40]. As shown in Fig. 6, it consists of a cascaded low-noise capacitive-feedback trans-impedance amplifier (TIA), capacitively-coupled to a current amplifier (CA). The TIA provides a low-impedance input for interfacing with a CMUT transducer, while the CA has a high-impedance output for driv-

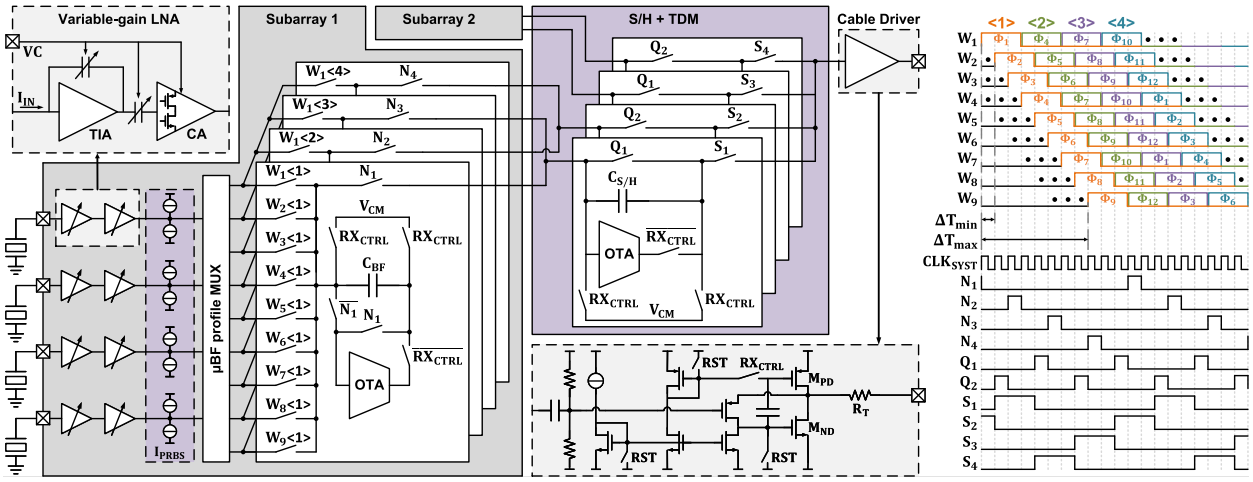

Fig. 6. Implementation of the RX front-end and the timing diagram of its delay-and-sum μBF and S/H + TDM stages.

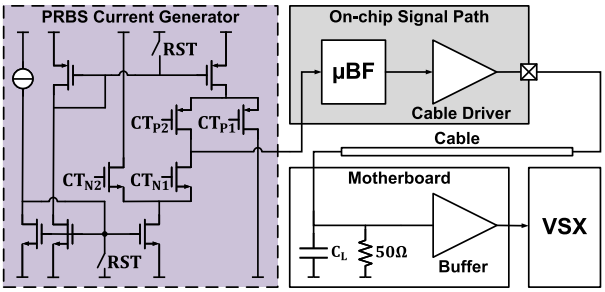

Fig. 7. Circuit diagram of the I_{PRBS} current source generating training data for the EQ in the system back-end and the signal path that is equalized.

ing the boxcar-integration-based μBF. Both stages implement half the total variable continuous gain range of 36 dB, which is controlled by a VC that is supplied per ASIC half. The VGA is scaled for an input-referred noise-density of 0.6 pA/$\sqrt{\text{Hz}}$ within a 1.4–3.8-MHz bandwidth at its maximum gain (VC = 1.2 V).

D. RX Channel-Count Reduction and Transmission

Fig. 6 shows the μBF and TDM circuit diagram. Like in [30], the boxcar-integration-based μBF consists of four time-interleaved integrator stages, followed by two ping-ponged sample-and-hold (S/H) stages. The current outputs of the four preceding CAs are steered to one of the four integrators in a cyclic fashion by means of input switches W_{1-9} ⟨1:4⟩. The phases for the clocks driving W_{1-9} ⟨1:4⟩ are programmable, while the integrator output charge is transferred to the S/H stages at a fixed cyclic timing via clock signals N_{1-4} and Q_{1-2}. The S/H stage that is not in charge-transfer mode is connected to the output, following clock signals S_{1-4}. As the timing for the integrators and charge-transfer is fixed, but the timing of the input currents can be shifted, the relative delay between input integration and output S/H is programmable for each input channel. Thus, a sum-and-delay operation is realized.

Since switched S/H stages define the RX channel output, TDM is easily realized by having four S/H stages drive the input of the following cable driver instead of 2. Conceptually, more than 2× TDM could be realized by interleaving more stages, but the channel-bandwidth of the targeted VSX back-end limits this design freedom. The cable driver is a super source follower with a class-AB driver [41]. Like the LNA and μBF OTAs, the class-AB driver has a sampled-and-held bias that is reset every T/R cycle by the RX_{CTRL} signal. M_{PD}, M_{ND}, and R_T are scaled to achieve a 50 Ω output impedance.

E. Channel Equalization and Calibration

To reduce TDM channel crosstalk, after digitizing the RX channels in the VSX, equalization is applied to flatten the frequency response. This technique is based on what was demonstrated in [25]. The EQs are implemented as adaptive linear EQs (ALEs) from the MATLAB communications library [42]. This is a FIR filter that uses the least-mean-square algorithm to scale its coefficients.

The training data for each RX channel EQ is generated on-chip with a programmable two-level current source I_{PRBS} at each μBF input. The implementation of the current sources is shown in Fig. 7. They output an off-chip supplied PRBS, which propagates through the on-chip μBF and cable driver, and the off-chip cable and buffer before being digitized by the VSX in the system back-end.

In addition to calibrating bandwidth-limitations, the system also calibrates static ripple signals at each RX channel output, resulting from switching artifacts introduced by the μBF. This is done by first collecting averaged RX channel data without an input signal, which only contains the ripple. This ripple is then subtracted from both the RX signals collected during imaging and the training data for the EQ.

IV. System Integration

A. CMUT Integration

As mentioned in Section II, the CMUTs are biased at a voltage V_B of +120 V to reliably operate in collapse mode. The CMUT top electrodes [see Fig. 1(c)] are routed to the ASIC periphery to be bonded to the PCB that provides V_B. Fig. 8(a) shows the applied biasing scheme. The CMUTs in every two columns of an ASIC half share one biasing pad. This allows only a section of the array to be disconnected if one or multiple CMUTs are faulty. Bias capacitor C_B provides an ac ground for the CMUTs, whereas the HV supply only operates as a dc bias source by means of resistor R_B. As both the sensitivity and center frequency of the CMUTs depend on V_B

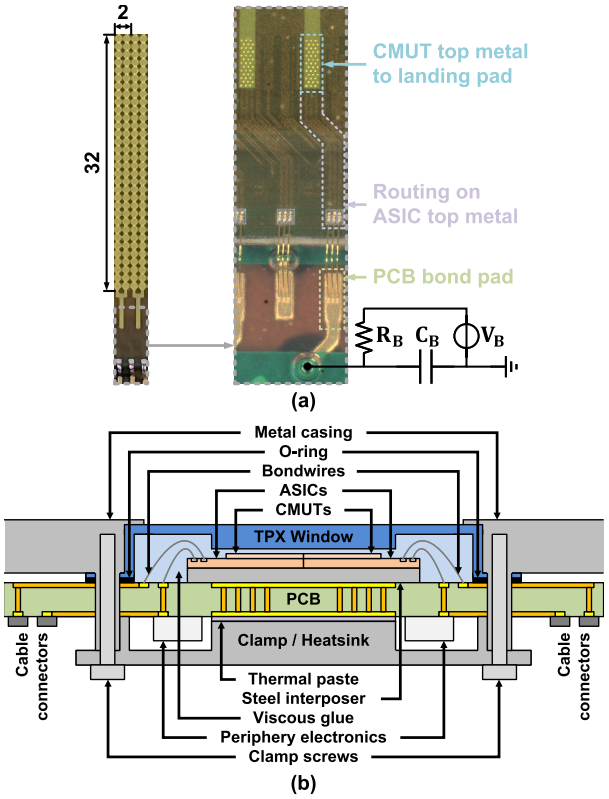

Fig. 8. (a) Overview of the CMUT biasing per two columns of the imaging array. (b) Overview of the system packaging.

[36], independent biasing of CMUT columns along the x-axis of the array enables apodization. However, this is not done in the presented system, where $V_B = +120$ V for simplicity.

To accommodate the CMUT devices on the standard TSMC BCD process wafers, a few layout restrictions were introduced. The microfabrication of the CMUTs requires a wafer surface topography that is as flat as possible. While the CMUT fabrication contains a planarization step, the top-metal thickness of the ASICs was also restricted as a precaution to improve the initial surface flatness, which added additional constraints to its power distribution design. In addition, sufficient spacing is required all-around any in-ASIC CMUT bias trace to prevent dielectric breakdown, as the TSMC 180-nm BCD process is not designed for trace-to-trace potential differences beyond 70 V.

B. Acoustic Packaging

To avoid excessive energy loss in both TX and RX, acoustic impedance matching of the array to the medium of interest is necessary. This requires a package with a similar impedance to water, while providing a water-tight seal for the underlying electronics. In addition, the surface of the imaging aperture must be flat to ensure a good contact with the medium of interest. Fig. 8(b) shows the designed package to meet these requirements.

The tiles are glued on an interposer plate that both ensures a flat imaging aperture and provides good thermal coupling to a PCB. After bonding the tiles to the PCB, a viscous glue is applied to the imaging array. This glue has a similar acoustic impedance to water while being electrically isolating. A polymethylpentene (TPX) window is then mounted on the

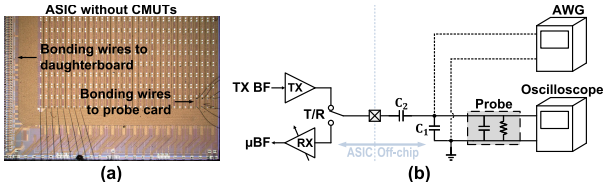

Fig. 9. (a) Picture of one of the ASICs without CMUTs connected to a probe card. (b) Diagram of the measurement setup for one input channel.

array, pushing the glue outwards, and coupling the array to the window while sealing the bonding wires. To ensure water-tightness around the window, the PCB is mounted in an anodized-aluminum casing, where an O-ring provides the water-tight seal. Pressure is applied to the O-ring via a backside clamp that also functions as a heatsink for the ASICs.

V. Experimental Results and Discussion

A. General Measurement Setup

As shown in Figs. 8(b) and 9(a), each tile in the probe is bonded to a daughterboard PCB. In the measurements presented, the digital inputs and RX output channels of 1 tile are connected via 1.65-m Samtec micro-coax cables with HQCD connectors [43] to the system back-end. The FPGA module that programs the tile is a DE10-Nano evaluation board [44] and the RX channel buffers on the motherboard in the system back-end are high-speed op-amps [45] configured as voltage followers with 50-Ω input termination. In addition to voltage regulation on the motherboard by means of linear-dropout regulators (LDOs), the analog supply is also regulated on the daughterboard to avoid TGC-related IR drop in the cables affecting the ASIC performance.

B. Electrical Characterization

ASICs without the monolithically-integrated CMUTs were used to validate both the electrical performance of the TX pulser and the RX front-ends. Selected transducer pads were bonded to a custom probe card. An overview of this measurement setup is shown in Fig. 9(b). C_1, C_2 and the input capacitance of the 200-MHz passive probe approximate the load of a CMUT, while also attenuating the voltage from the HV TX pulsers on the ASIC by 13.4×. This attenuation was calibrated and corrected for in TX measurements. The oscilloscope is connected for both TX and RX measurements, but the AWG is only connected for RX.

Fig. 10(a) shows the probed pulser output when transmitting various PDM waveforms at the maximum TX voltage of 65 V. The two-period pulse is used for most standard imaging applications, but chirps or pseudorandom sequences can be used instead to increase the contrast from low-reflective objects, as these waveforms contain more energy. Fig. 10(b) shows the corresponding acoustic outputs, which are covered in more detail in Section V-C. Fig. 11 shows the pulser output when transmitting the same chirp as shown in Fig. 10(a) after being delayed between 0 and $8T_{SYST}$ by the TX BF. Combining the results from Figs. 10 and 11 demonstrates the ability to BF arbitrary PDM waveforms.

Fig. 12(a) shows the subarray gain versus frequency for multiple TGC VC settings. Fig. 12(b) shows the gain at the 2.6-MHz center frequency and −3-dB BW versus VC.

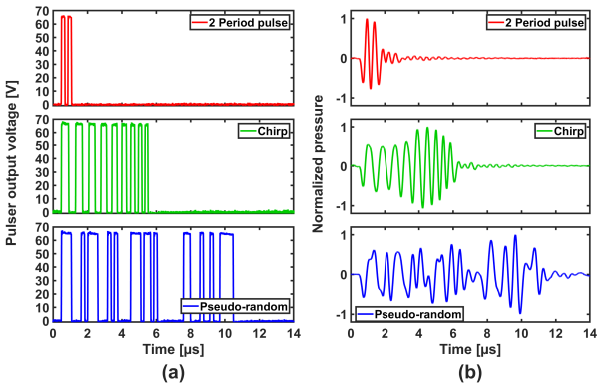

Fig. 10. (a) Transducer pad output for various PDM signals at the maximum ASIC TX amplitude. (b) Normalized transmitted acoustic signal corresponding to the transducer pad signals at a 40-V TX amplitude.

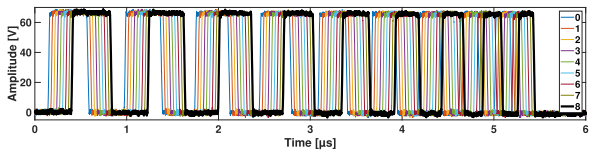

Fig. 11. Pulser outputting a chirp sequence, shifted between 0 and $8T_{SYST}$ by the TX BF.

The gain range is 36 dB and the BW varies from 3.0 to 3.8 MHz across VC. Given a 1.4–3.8-MHz BW of interest and 2.6-MHz center frequency defined by the CMUTs, the fractional bandwidth of the amplifier varies from ∼60% to ∼90%, which is more than the required 50% across the gain range. These results also approximate the same attenuation that will occur for the CMUT-to-LNA input current, as the impedance of C_2 is similar to that of the CMUT.

To validate the subgroup crosstalk, test signals are applied to an RX channel [see Fig. 9(a)]. The EQs applied for the crosstalk measurements and imaging results (see Section V-D) have 18 taps. They equalize the VSX 14-bit ADC output data, which is sampled at 3× the TDM frequency at 62.5 MHz. As such, the EQs are configured fractionally spaced, using three samples per symbol. They are trained with a 2500-times-repeated 16 382-bit PRBS.

Fig. 13(a) and (b) shows the crosstalk from subarray 1 to subarray 2 and vice-versa with and without back-end equalization in the time domain. The test signals are 2.6-MHz-center-frequency two-period pulses. With equalization applied, the peak-peak crosstalk from subarray 1 to subarray 2 improves from −11.4 to −20.9 dB and from subarray 2 to subarray 1 from −10.9 to −21.4 dB.

Fig. 13(c) and (d) shows the power spectral density (PSD) of the RX channel output when a 2.5-MHz tone is applied to the subarray inputs. The reduction in a μBF-induced ripple tone at 2.6 MHz is also shown after calibration. Fig. 13(e) and (f) shows the crosstalk improvement when the frequency of the input tone is swept across the 1.4–3.8-MHz bandwidth of interest. The effectiveness of the equalization varies over frequency, but the average crosstalk from subarray 1 to subarray 2 improves to −22.4 dB, and the average crosstalk from subarray 2 to subarray 1 to −25.7 dB.

As the power dissipation of the pulser is directly related to the pulse transmission density, Fig. 14(a) shows the dissipation versus the number of transmitted pulse periods when an ASIC

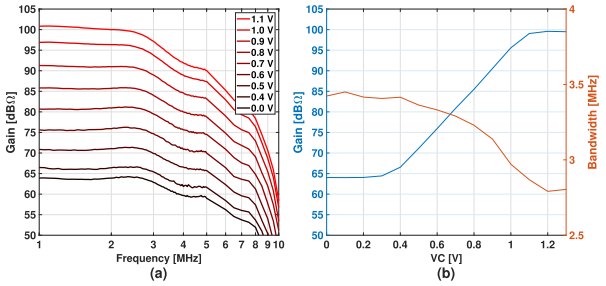

Fig. 12. (a) Measured RX channel gain versus frequency for various VC settings. (b) Gain at 2.6 MHz and −3-dB BW versus the VC control voltage.

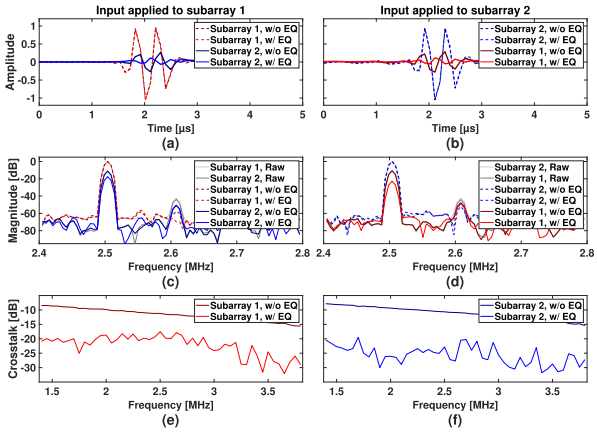

Fig. 13. (a) Crosstalk from a pulse into subarray 1 to subarray 2. (b) Crosstalk from a pulse into subarray 2 to subarray 1. (c) Crosstalk from a 2.5-MHz tone into subarray 1 to subarray 2. (d) Crosstalk from a 2.5-MHz tone into subarray 2 to subarray 1. (e) Crosstalk from tones within the bandwidth of interest into subarray 1 to subarray 2. (f) Crosstalk from tones within the bandwidth of interest into subarray 2 to subarray 1.

half is transmitting with no TX BF delays. This is shown for a prototype with and without CMUTs. As most imaging modes using this probe TX a two-period pulse per T/R cycle, the typical number of pulse periods/second is 16 000 when imaging at 2000 volumes/s with four diverging waves per volume. The associated power/element drawn from the HV supply is 186 μW, which is much lower than the RX power dissipation.

A breakdown of the power dissipation of the probe is shown in Fig. 14(b). All power dissipation was measured during active operation using a prototype with CMUTs. The PRF is 8 kHz, as needed for 2000 volumes/s imaging. However, to measure different parts of the RX circuitry independently, parts of the ASIC were disabled. The RX front-end dissipates 0.79 mW/El. When applying a ramp function to VC during each T/R cycle.

A breakdown of the ASIC area is shown in Fig. 14(c). Although active circuits use most areas, because of the pad-limited nature of the design, a substantial 44% of the total area consists of bond pads, pad protection circuitry, decoupling capacitors, and interconnect. Of the active design, the RX front-end dominates with 36% of the total area, while the combined TX circuit only uses 15% of the total area.

C. Acoustic Characterization

Fig. 15 shows the measurement setup for the acoustic measurements. A 3-D-printed water tank is placed on top of the ultrasound probe. The interface between the two consists of acoustic gel and a plastic bag with a thickness much lower than

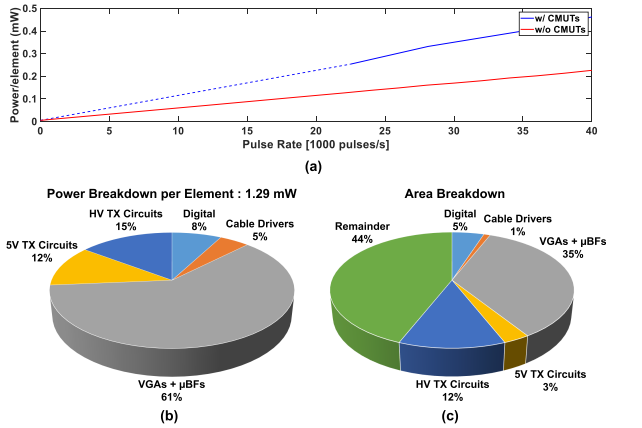

Fig. 14. (a) Relation between the HV supply power/element and the number of pulse periods transmitted, using a repeated chirp sequence as a test signal (see Fig. 10). The solid sections of the line are measured data points, while the dotted sections are from interpolation. (b) Element-referred power breakdown for 16 kperiods/s TX and VC ramping per T/R cycle. (c) Area breakdown of the tiles. The "remainder" category contains decoupling capacitors, bond pads, interconnect, ESD protection circuits, and unused areas.

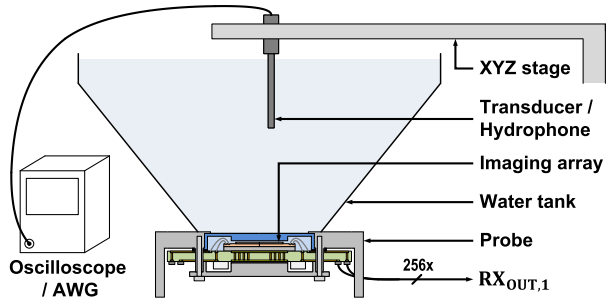

Fig. 15. Acoustic measurement setup.

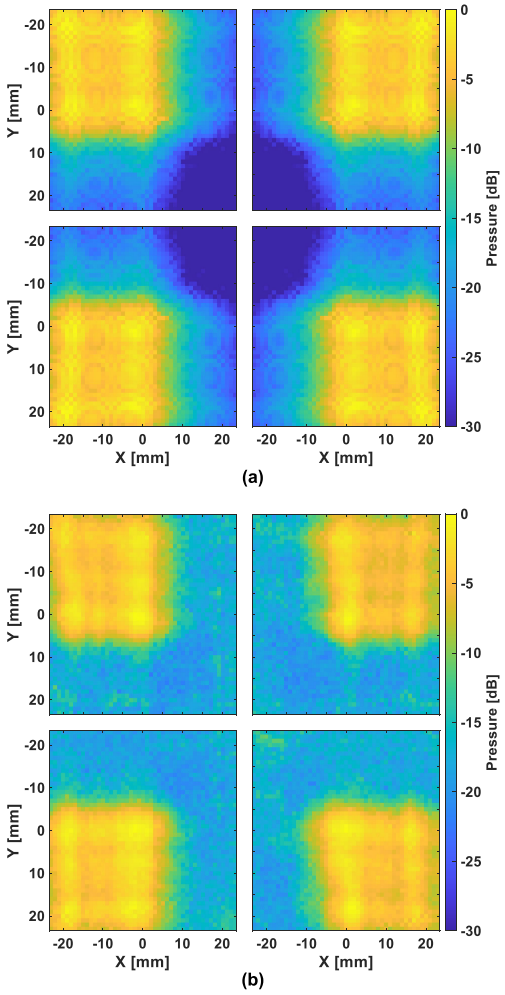

Fig. 16. (a) Simulated C-planes at 3.5 cm from the probe for the diverging waves used in the TX scheme for imaging of 60° × 60° × 10 cm at 2000 volumes/s. (b) Measured C-planes of the same TX waves at 3.5 cm from the probe.

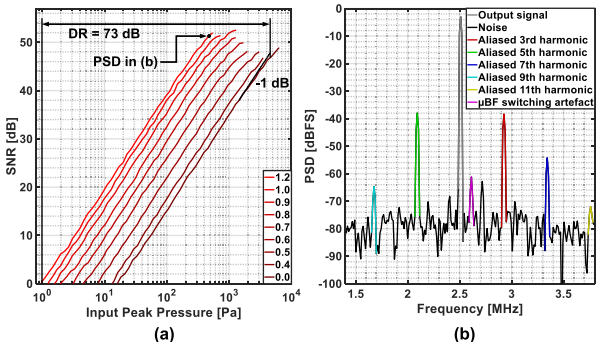

Fig. 17. (a) Subarray SNR versus input peak pressure for varying VC control voltages. (b) Example PSD of the output signal at high signal levels.

the 600-μm nominal wavelength of the ultrasound waves, thus not significantly attenuating signals. From the top of the water tank, an xyz stage with a holder positions imaging objects or instrumentation, depending on the measurement.

Fig. 10(b) shows the measured normalized pressure of the transmitted waveforms using the driving signals shown in Fig. 10(a). All elements on 1 tile were transmitting with no time delays. The waveforms were transmitted at the nominal maximum of the probe, where TX is limited to 40 V. As is shown, the probe is capable of producing a wide range of acoustic waveforms by means of the arbitrary PDM driving signal for the CMUTs.

Fig. 16 demonstrates the TX BF functionality by comparing four scanned C-planes of TX beams with their ideal Field II [46] simulation result. These diverging beams are the same as used in the TX scheme for 60° × 60° × 10 cm 2000 volumes/s imaging. As the results are presented for 1 tile, the imaging scheme only uses the central 32 × 32 elements, as a symmetrical TX aperture is needed to create the desired symmetrical diverging waves.

The ASIC was configured to cycle through nine pre-uploaded TX profiles, as it also does for HVR imaging. The C-plane has a 3.5 cm distance from the array. The peak-peak pressures were measured using a 200-μm diameter hydrophone and an xyz stage, scanning a grid of 4.6 × 4.6 cm with 1-mm steps. The PRF of the ASIC during this measurement is 18 kHz. As shown, the measured diverging waves are in good agreement with the simulations. The elevated clutter is from reflections in the water tank, originating from prior scan point transmissions.

Fig. 17(a) shows the output SNR versus the peak input pressure of a subarray for varying VC control voltages. The lowest signal level is at an SNR of 0 dB in the highest gain setting. The highest signal level is at the point where the SNR diverges 1 dB from the dB-linear SNR-to-pressure curve at the lowest gain setting. In total, the measurable peak pressure range is between 0.99 and 4559 Pa, which gives a 73-dB DR. The peak SNR is 52 dB and was measured at the highest gain

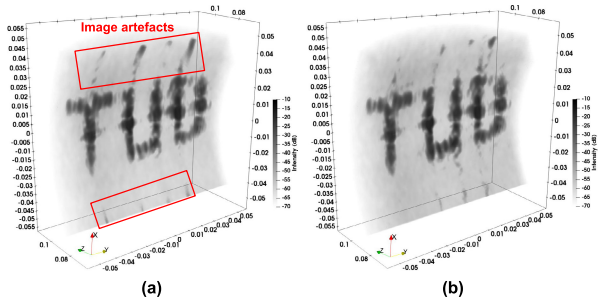

Fig. 18. (a) 3-D B-mode image of 3-D-printed "TUD" logo without equalization. (b) 3-D B-mode image of the same 3-D-printed "TUD" logo with equalization.

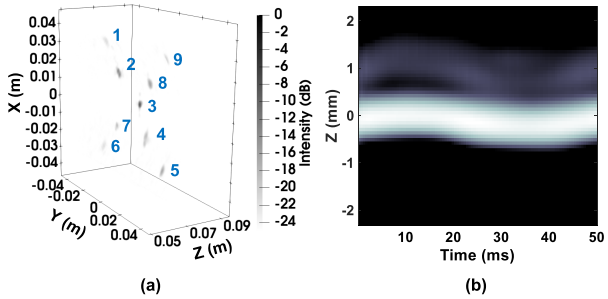

Fig. 19. (a) 3-D B-mode image of cross-shaped needle phantom. (b) M-mode image of needle 3, which is moving along the Z-axis at a 20-Hz frequency.

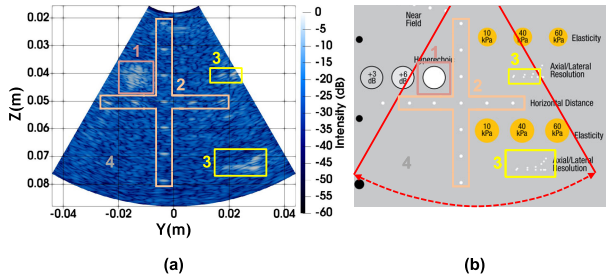

Fig. 20. (a) B-mode image of tissue mimicking (CIRS 040GSE) phantom. Region 1 shows a hyperechoic cylinder, region 2 shows nylon strings, region 3 shows nylon strings with a smaller size, and region 4 shows the background speckle of the phantom. (b) Reference image of the phantom [47].

setting. Distortion of the RX signals does not significantly affect the image quality, as received pulse amplitudes, widths and times-of-arrival define the reconstructed image. Therefore, SNR is used as a metric for DR instead of the signal-to-noise + distortion ratio (SNDR).

Given that the SNR is 0 dB for a peak input pressure of 0.99 Pa, the input pressure noise is calculated to be 0.452 $\text{mPa}_{\text{rms}}/\sqrt{\text{Hz}}$ in the 1.4–3.8-MHz bandwidth of interest. The simulated conversion efficiency of the CMUTs is between 2.5 and 4.0 nA/Pa. When combining this conversion efficiency with the estimated measurement uncertainties of the acoustic measurement setup, the input-referred current noise density is estimated at 1.4 $\text{pA}_{\text{rms}}/\sqrt{\text{Hz}}$ with an uncertainty of ± 0.7 $\text{pA}_{\text{rms}}/\sqrt{\text{Hz}}$, which is in line with expectations. Fig. 17(b) shows the output PSD used for deriving one data point in Fig. 17(a). The signal tone is at 2.5 MHz. At high amplitudes, odd-harmonics that alias back into the bandwidth of interest dominate distortion.

D. Imaging Results

To demonstrate the imaging capabilities of the probe, images were made of a tissue-mimicking phantom (CIRS 040GSE) [47] and multiple objects in a water tank. The 3-D images shown in Figs. 18 and 19 were made with 1 tile, using the same TX scheme as is shown in Fig. 16 in the same water tank, using a 5-V TX amplitude. Fig. 18 shows a 60° × 60° × 10-cm-volume 3-D B-mode image of 3-D-printed "TUD" logo with and without channel equalization. As the images demonstrate, the artifacts in the image are reduced with decreased TDM-induced crosstalk.

Fig. 19(a) shows a similarly obtained 3-D B-mode image of a set of needle heads, connected to a shaker, which oscillated the needles along the Z-axis at 20 Hz. Given that the probe is imaging at 2000 volumes/s, it is oversampling the needle head positions by 50×, as is demonstrated in Fig. 19(b) where the position of center needle 3 is shown versus time.

Fig. 20 shows a B-mode image of the tissue-mimicking phantom, which attenuates ultrasound waves by 0.5 dB/cm/MHz. To reconstruct the image, three beams were used that are diverging along the Y-axis and plane waves along the out-of-plane X-axis, rather than the transmission scheme shown in Fig. 16. Just like that scheme, only the center square is used in TX for the same reason. The opening angle of the TX beams is also the same along the Y-axis. The image was recorded at 8000/3 ≈ 2.7 kHz at a 5-V TX. This lower TX voltage was chosen as a precaution to prevent damaging the limited number of imaging prototypes available. Despite this, the probe has enough round-trip DR to obtain a penetration depth of ≥8.8 cm with a sufficiently high contrast. This gives ample margin for features that have lower contrast when imaging with 40-V TX. Note that the imaging depth is limited by the depth that the VSX can process at an 8-kHz PRF, which is roughly 7 mm less than the theoretically achievable depth at a 1540 m/s speed of sound in human tissue.

VI. Conclusion

To address the emerging need for large-volume HVR imaging, this article has presented a 4096-element 3-D ultrasound probe. The probe is based on 365-μm-pitch CMUTs with a 2.6-MHz center-frequency, which are monolithically integrated on 2 tiled ASICs that were fabricated in a 180-nm BCD process. For TX, these contain a novel arbitrary-PDM-wave TX BF, implemented as a programmable digital pipeline. It interfaces with element-level two-level 65-V unipolar pulsers that drive the CMUT array. In RX, the ASICs pre-amplify signals with element-level low-noise VGAs with a 36-dB gain range and provide 8× channel-count reduction by applying 2 × 2 μBF and 2× TDM. Together, the proposed system architecture enables imaging a 60° × 60° × 10-cm volume at 2000 volumes/s, the highest volume rate for designs with in-probe channel-count reduction reported to date, while providing sufficient RX-channel reduction for the probe to interface with existing imaging systems. Moreover, PRBS-trained EQ reduces RX-channel crosstalk, which allows power-efficient scaling of the in-probe cable drivers. A set of prototypes has

TABLE I
PERFORMANCE SUMMARY AND COMPARISON WITH THE PRIOR ART

	This work	[18]	[31]	[14]	[15]	[17]
Technology	**180 nm BCD + MEMS**	180 nm BCD + MEMS	180 nm BCD	180 nm BCD	180 nm BCD	180 nm BCD
Transducer	**2D CMUT**	2D CMUT	2D PZT	2D PZT	CMUT	2D PZT
TX/RX Channels	**4096 / 4096**	8960 / 8960	128 / 3072	288 / 288	40 / 40	256 / 256
Centre Frequency	**2.6 MHz**	5.5 MHz	2 MHz	6 MHz	5 MHz	9 MHz
Element Pitch	**365 µm**	208 µm	300 µm	160 µm	N/A	125 µm
Arbitrary-Wave TX	✓	✓	×	×	×	×
TX BF	✓	✓	✓	✓	✓	✓
Crosstalk Calibration	✓	×	×	×	×	×
Volume Rate [vol/s]	**2000**	N/A	N/A	1000	N/A	N/A
Channel Reduction	**8×**	64×	24×	18×	40×	128×
Channel Reduction Method(s)[*1]	**4× µBF** **2× TDM**	8× Summing / MUX 8× RX Pre-processing[*2]	24× µBF	3× µBF 6× D-TDM	5× µBF 8× TDM	8× MUX 4× µBF 4× D-TDM
RX Output Type	**Analog**	Digital	Analog	Digital	Analog	Digital
Max TX Voltage [V]	**65**[*3]	50	138	30	70	20
Active Area / El. [mm^2]	**0.12**[*4]	0.043	0.09	0.03	0.15	0.016
RX Power / El. [mW]	**0.85**[*5]	0.66[*6]	0.74	1.12	4.65	1.83
Peak SNR [dB]	**52**	54.5[*6]	N/A	52.2	N/A	54
Input DR [dB]	**73**	N/A	85	91	76	83

*1 : micro-beamformer (µBF), analog time-division multiplexing (TDM), multiplexing (MUX), digital time-division multiplexing (D-TDM)
*2 : A combination of signal-processing techniques to realize channel-count reduction.
*3 : Voltage can be generated by the ASICs, but the acoustic prototypes are limited to 40 V TX.
*4 : This excludes the 'Remainder' category from Fig. 14.
*5 : Given a ramp function applied to VC over each T/R period. RX Power per Element consists of the power consumed by the VGAs, µBFs and cable drivers divided by the number of elements.
*6 : From the results presented in [48].

been developed for both electrical and acoustic performance evaluation. With the acoustic prototypes, the targeted imaging performance was demonstrated with both water tank measurements and tissue-mimicking phantom images.

Table I shows a summary of the achieved results and a comparison with the prior art. While previous works have also reported combinations of μBF and signal modulation techniques to reduce channel count [14], [15], [17], this work demonstrates its scalability to imaging arrays with thousands of elements, while retaining a high volume rate. In addition, the system has a high flexibility in TX waveform definition at a reduced complexity compared to arbitrary-wave TX BFs in the prior art. Together with competitive power consumption and DR, it is a promising solution for use in medical R&D targeting improved diagnosis and treatment of AAAs, as well as other applications requiring HVR imaging of a large volume.

ACKNOWLEDGMENT

The authors thank B. Jacobs, J. Chacon, D. Mtsuko, E. Timmering, J. Klootwijk, and R. van Schaijk of Philips and T. Hosman and L. Pakula of TU Delft for their contributions.

REFERENCES

[1] V. Kessler, J. Klopf, W. Eilenberg, C. Neumayer, and C. Brostjan, "AAA revisited: A comprehensive review of risk factors, management, and hallmarks of pathogenesis," *Biomedicines*, vol. 10, no. 1, p. 94, Jan. 2022. [Online]. Available: https://www.mdpi.com/2227-9059/10/1/94

[2] A. Wanhainen et al., "Editor's choice—European society for vascular surgery (ESVS) 2019 clinical practice guidelines on the management of abdominal aorto-iliac artery aneurysms," *Eur. J. Vascular Endovascular Surg.*, vol. 57, no. 1, pp. 8–93, 2019. [Online]. Available: https://www.sciencedirect.com/science/article/pii/S1078588418306981

[3] L. C. Jansen, H.-M. Schwab, F. N. van de Vosse, M. R. H. M. van Sambeek, and R. G. P. Lopata, "Local and global distensibility assessment of abdominal aortic aneurysms in vivo from probe tracked 2D ultrasound images," *Frontiers Med. Technol.*, vol. 4, Jan. 2023, Art. no. 1052213, doi: 10.3389/fmedt.2022.1052213.

[4] L. C. Jansen, S. Fekkes, H.-M. Schwab, and R. G. P. Lopata, "Increasing abdominal aortic aneurysm curvature visibility using 3D dual probe bistatic ultrasound imaging combined with probe translation," *Ultrasonics*, vol. 139, Apr. 2024, Art. no. 107284. [Online]. Available: https://www.sciencedirect.com/science/article/pii/S0041624X24000465

[5] E. J. Maas, A. H. M. Nievergeld, J. H. C. Fonken, M. Thirugnanasambandam, M. R. H. M. van Sambeek, and R. G. P. Lopata, "3D-ultrasound based mechanical and geometrical analysis of abdominal aortic aneurysms and relationship to growth," *Ann. Biomed. Eng.*, vol. 51, no. 11, pp. 2554–2565, Nov. 2023.

[6] J. Voorneveld et al., "High-frame-rate contrast-enhanced ultrasound for velocimetry in the human abdominal aorta," *IEEE Trans. Ultrason., Ferroelectr., Freq. Control*, vol. 65, no. 12, pp. 2245–2254, Dec. 2018.

[7] K. Riemer, M. Toulemonde, E. M. Rowland, C. H. Leow, M. Tang, and P. D. Weinberg, "4D blood flow and wall shear stress measured using volumetric ultrasound image velocimetry," in *Proc. IEEE Int. Ultrason. Symp. (IUS)*, Sep. 2020, pp. 1–4.

[8] A. J. Y. Chee, T. Ishii, B. Y. S. Yiu, and A. C. H. Yu, "Helical toroid phantom for 3D flow imaging investigations," *Phys. Med. Biol.*, vol. 66, no. 4, Feb. 2021, Art. no. 045029, doi: 10.1088/1361-6560/abda99.

[9] J. Provost et al., "3D ultrafast ultrasound imaging in vivo," *Phys. Med. Biol.*, vol. 59, no. 19, pp. 1–13, Sep. 2014, doi: 10.1088/0031-9155/59/19/l1.

[10] A. Ramalli, E. Boni, A. S. Savoia, and P. Tortoli, "Density-tapered spiral arrays for ultrasound 3-D imaging," *IEEE Trans. Ultrason., Ferroelectr., Freq. Control*, vol. 62, no. 8, pp. 1580–1588, Aug. 2015.

[11] J. A. Jensen et al., "Anatomic and functional imaging using row-column arrays," *IEEE Trans. Ultrason., Ferroelectr., Freq. Control*, vol. 69, no. 10, pp. 2722–2738, Oct. 2022.

[12] P. Santos, G. U. Haugen, L. Løvstakken, E. Samset, and J. D'hooge, "Diverging wave volumetric imaging using subaperture beamforming," *IEEE Trans. Ultrason., Ferroelectr., Freq. Control*, vol. 63, no. 12, pp. 2114–2124, Dec. 2016.

[13] B. Savord and R. Solomon, "Fully sampled matrix transducer for real time 3D ultrasonic imaging," in *Proc. IEEE Symp. Ultrason.*, vol. 1, Oct. 2003, pp. 945–953.

[14] Y. M. Hopf et al., "A pitch-matched high-frame-rate ultrasound imaging ASIC for catheter-based 3-D probes," *IEEE J. Solid-State Circuits*, vol. 59, no. 2, pp. 476–491, Feb. 2024.

[15] A. Rezvanitabar et al., "Integrated hybrid sub-aperture beamforming and time-division multiplexing for massive readout in ultrasound imaging," *IEEE Trans. Biomed. Circuits Syst.*, vol. 16, no. 5, pp. 972–980, Oct. 2022.

[16] C. Chen et al., "A pitch-matched front-end ASIC with integrated subarray beamforming ADC for miniature 3-D ultrasound probes," *IEEE J. Solid-State Circuits*, vol. 53, no. 11, pp. 3050–3064, Nov. 2018.
[17] P. Guo et al., "A 125 μm-pitch-matched transceiver ASIC with micro-beamforming ADC and multi-level signaling for 3-D trans-fontanelle ultrasonography," *IEEE J. Solid-State Circuits*, vol. 59, no. 6, pp. 2604–2617, Aug. 2024.
[18] J. M. Rothberg et al., "Ultrasound-on-chip platform for medical imaging, analysis, and collective intelligence," *Proc. Nat. Acad. Sci. USA*, vol. 118, no. 27, Jul. 2021, Art. no. 2019339118.
[19] R. Wodnicki et al., "Row-multiplexed 1,024 element large aperture array for electronic scanning in elevation," in *Proc. IEEE Int. Ultrason. Symp. (IUS)*, Oct. 2022, pp. 1–4.
[20] T. Kim et al., "Design of an ultrasound transceiver ASIC with a switching-artifact reduction technique for 3D carotid artery imaging," *Sensors*, vol. 21, no. 1, p. 150, Dec. 2020. [Online]. Available: https://www.mdpi.com/1424-8220/21/1/150
[21] S. I. Nikolov, J. Kortbek, and J. A. Jensen, "Practical applications of synthetic aperture imaging," in *Proc. IEEE Int. Ultrason. Symp.*, Oct. 2010, pp. 350–358.
[22] J. A. Jensen, "Estimation of high velocities in synthetic-aperture imaging—Part I: Theory," *IEEE Trans. Ultrason., Ferroelectr., Freq. Control*, vol. 66, no. 6, pp. 1024–1031, Jun. 2019.
[23] P. Wagner, C. Daft, S. Panda, and I. Ladabaum, "5G-1 two approaches to electronically scanned 3D imaging using cMUTs," in *Proc. IEEE Ultrason. Symp.*, Oct. 2006, pp. 685–688.
[24] T. M. Carpenter, M. W. Rashid, M. Ghovanloo, D. M. J. Cowell, S. Freear, and F. L. Degertekin, "Direct digital demultiplexing of analog TDM signals for cable reduction in ultrasound imaging catheters," *IEEE Trans. Ultrason., Ferroelectr., Freq. Control*, vol. 63, no. 8, pp. 1078–1085, Aug. 2016.
[25] Q. Liu, C. Chen, Z.-Y. Chang, C. Prins, and M. A. P. Pertijs, "A mixed-signal multiplexing system for cable-count reduction in ultrasound probes," in *Proc. IEEE Int. Ultrason. Symp. (IUS)*, Oct. 2015, pp. 1–4.
[26] M. W. Rashid, C. Tekes, M. Ghovanloo, and F. L. Degertekin, "Design of frequency-division multiplexing front-end receiver electronics for CMUT-on-CMOS based intracardiac echocardiography," in *Proc. IEEE Int. Ultrason. Symp.*, Sep. 2014, pp. 1540–1543.
[27] *Vantage Specifications for Biomedical & General Applications*, Verasonics, Kirkland, Washington, 2024.
[28] E. Boni et al., "ULA-OP 256: A 256-channel open scanner for development and real-time implementation of new ultrasound methods," *IEEE Trans. Ultrason., Ferroelectr., Freq. Control*, vol. 63, no. 10, pp. 1488–1495, Oct. 2016.
[29] Y. M. Hopf et al., "A pitch-matched transceiver ASIC with shared hybrid beamforming ADC for high-frame-rate 3-D intracardiac echocardiography," *IEEE J. Solid-State Circuits*, vol. 57, no. 11, pp. 3228–3242, Nov. 2022.
[30] P. Guo et al., "A 1.2-mW/channel pitch-matched transceiver ASIC employing a boxcar-integration-based RX micro-beamformer for high-resolution 3-D ultrasound imaging," *IEEE J. Solid-State Circuits*, vol. 58, no. 9, pp. 2607–2618, Sep. 2023.
[31] Y. Igarashi et al., "Single-chip 3072-element-channel transceiver/128-subarray-channel 2-D array IC with analog RX and all-digital TX beamformer for echocardiography," *IEEE J. Solid-State Circuits*, vol. 54, no. 9, pp. 2555–2567, Sep. 2019.
[32] A. Ramalli, A. Dallai, E. Boni, F. Guidi, S. Ricci, and P. Tortoli, "Real-time pulse compression in multigate spectral Doppler imaging," in *Proc. IEEE Int. Ultrason. Symp. (IUS)*, Oct. 2015, pp. 1–4.
[33] P. Song, M. W. Urban, A. Manduca, J. F. Greenleaf, and S. Chen, "Coded excitation plane wave imaging for shear wave motion detection," *IEEE Trans. Ultrason., Ferroelectr., Freq. Control*, vol. 62, no. 7, pp. 1356–1372, Jul. 2015.
[34] J. Voorneveld et al., "4-D echo-particle image velocimetry in a left ventricular phantom," *Ultrasound Med. Biol.*, vol. 46, no. 3, pp. 805–817, Mar. 2020. [Online]. Available: https://www.sciencedirect.com/science/article/pii/S0301562919316217
[35] M. S. Kilinc, H. Lee, C. D. Arvanitis, and F. L. Degertekin, "Dual mode CMUT array operation for skull imaging and passive acoustic monitoring in transcranial ultrasound," in *Proc. IEEE Int. Ultrason. Symp. (IUS)*, Sep. 2021, pp. 1–4.
[36] R. Van Schaijk and M. Devices, "CMUT: A versatile and low cost ultrasonic platform," in *Micromachined Ultrasonic Transducers*. Philips Innovation Services, 2019. [Online]. Available: https://www.salland.com/wp-content/uploads/2019/06/11-Rob-van-Schaijk-Philips-InS-MEMS-Seminar-2019.pdf
[37] Y. M. Hopf et al., "A compact integrated high-voltage pulser insensitive to supply transients for 3-D miniature ultrasound probes," *IEEE Solid-State Circuits Lett.*, vol. 5, pp. 166–169, 2022.
[38] M. Tan et al., "A 64-channel transmit beamformer with ±30-V bipolar high-voltage pulsers for catheter-based ultrasound probes," *IEEE J. Solid-State Circuits*, vol. 55, no. 7, pp. 1796–1806, Jul. 2020.
[39] H. Zhang et al., "A high-linearity and low-EMI multilevel class-D amplifier," *IEEE J. Solid-State Circuits*, vol. 56, no. 4, pp. 1176–1185, Apr. 2021.
[40] P. Guo et al., "A pitch-matched low-noise analog front-end with accurate continuous time-gain compensation for high-density ultrasound transducer arrays," *IEEE J. Solid-State Circuits*, vol. 58, no. 6, pp. 1693–1705, Jun. 2023.
[41] E. Kang et al., "A reconfigurable ultrasound transceiver ASIC with 24×40 elements for 3-D carotid artery imaging," *IEEE J. Solid-State Circuits*, vol. 53, no. 7, pp. 2065–2075, Jul. 2018.
[42] MathWorks. *Adaptive Equalizers*. Accessed: Feb. 3, 2025. [Online]. Available: https://nl.mathworks.com/help/comm/ug/adaptive-equalizers.html
[43] Samtec. *HQCD*. Accessed: Feb. 3, 2025. [Online]. Available: https://www.samtec.com/products/hqcd
[44] Terasic. *DE10-Nano Kit*. Accessed: Feb. 3, 2025. [Online]. Available: https://www.terasic.com.tw/cgi-bin/page/archive.pl?Language=English&CategoryNo=167&No=1046&PartNo=2#heading
[45] T-Instruments, *OPAx354-Q1 250-MHz, Rail-to-Rail I/O, CMOS Operation Amplifiers*, Texas Instrum., 2018. Accessed: Feb. 3, 2025. [Online]. Available: https://www.ti.com/lit/ds/symlink/opa4354-q1.pdf?HQS=TI-null-null-alldatasheets-df-pf-SEP-wwe&ts=1730713860935
[46] J. A. Jensen. *Field-II Simulation Program*. Accessed: Feb. 3, 2025. [Online]. Available: https://field-ii.dk/
[47] CIRS. *Multi-Purpose, Multi-Tissue Ultrasound Phantom Model 040GSE*. Accessed: Feb. 3, 2025. [Online]. Available: https://www.cirsinc.com/wp-content/uploads/2021/09/040GSE-DS-093021.pdf
[48] N. Sanchez et al., "An 8960-element ultrasound-on-chip for point-of-care ultrasound," in *IEEE Int. Solid-State Circuits Conf. (ISSCC) Dig. Tech. Papers*, vol. 64, Feb. 2021, pp. 480–482.

Nuriel N. M. Rozsa (Member, IEEE) received the B.Sc. degree (cum laude) in electrical engineering and the B.Sc. honours program certificate from Delft University of Technology, Delft, The Netherlands, in 2018, and the M.Sc. degree in microelectronics from Delft University of Technology, in 2021. He is currently pursuing the Ph.D. degree with the Electronic Instrumentation Laboratory, working within the Ultra-X-Treme research program on high frame-rate 3-D ultrasound probes for imaging the Abdominal Aorta.

His current research interests include analog and mixed-signal electronics design for ultrasound imaging applications.

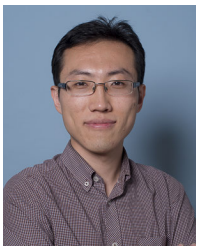

Zhao Chen (Member, IEEE) received the B.S. degree in microelectronics from Fudan University, Shanghai, China, in 2011, and the M.S. degree in electrical and electronic engineering from Imperial College London, U.K., in 2012. From 2014 to 2020, he pursued the Ph.D. degree in electrical engineering at Delft University of Technology, Delft, The Netherlands, where his research focused on ASIC design for 3D medical ultrasound imaging.

After obtaining his Ph.D., he joined Philips Research, The Netherlands, as an Analog and Mixed-Signal IC Designer. In 2024, he transitioned to Robert Bosch GmbH, Reutlingen, Germany. His research interests include analog and mixed-signal electronics, with a particular focus on biomedical and automotive applications.

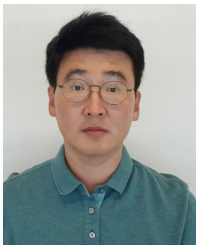

Taehoon Kim (Member, IEEE) received the B.S., M.S., and Ph.D. degrees in electrical engineering and computer science from Seoul National University, Seoul, South Korea, in 2009, 2012, and 2017, respectively.

From 2017 to 2018, he was part of the ASIC and IP Development Team at Samsung Electronics, Hwasung, South Korea. He then pursued Post-Doctoral Research at the Electronic Instrumentation Laboratory, Delft University of Technology, Delft, The Netherlands, from 2018 to 2021. Since 2022, he has been an Electronics Engineer with the Electronics Technology Group, Jet Propulsion Laboratory, California Institute of Technology, Pasadena, CA, USA. His research interests include integrated circuit design for advanced detector technologies in space instrumentation.

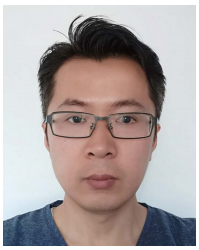

Peng Guo (Member, IEEE) received the M.Sc. degree in microelectronics from Zhejiang University, Hangzhou, China, in 2006, and the Ph.D. degree in electrical engineering from Delft University of Technology (TU Delft), Delft, The Netherlands, in 2023.

Since 2006, he has been working in the industry, focusing primarily on low-power and low-noise sensor-related ASIC system design, which includes accelerometers, gyroscopes, and e-compasses. In 2018, he joined the Electronic Instrumentation Laboratory at TU Delft, where his research was centered around ASIC design for ultrasound imaging, and he joined Bioelectronics as a Post-Doctoral Researcher in 2023. His research now revolves around ultrasound neuromodulation and the associated ASIC design.

Yannick M. Hopf (Member, IEEE) received the B.Sc. and M.Sc. degrees (cum laude) in electrical engineering from the Technical University of Darmstadt, Darmstadt, Germany, in 2014 and 2017, respectively, and the Ph.D. degree in electrical engineering from the Electronic Instrumentation Laboratory, Delft University of Technology, Delft, The Netherlands, in 2023, with a focus on application-specific integrated circuit (ASIC) design for 3-D high-frame-rate medical ultrasound imaging.

He is currently working with Sonosilicon, Delft, as a Senior Analog Design Engineer to provide ASIC solutions for the next generation of medical ultrasound devices. His current research interests include analog and mixed-signal integrated circuits for ultrasound imaging, high-voltage electronics, and low-power analog-to-digital converters.

Dr. Hopf was a recipient of the Eckelmann AG Price for best M.Sc. degree in his year, the ProRISC 2022 Best Presentation Award, and the 2023 SSCS Predoctoral Achievement Award.

Jason Voorneveld (Member, IEEE) was born in Johannesburg, South Africa, in 1987. He received the B.Sc. degree in electromechanical engineering and the M.Sc. degree in biomedical engineering from the University of Cape Town, Cape Town, South Africa, in 2009 and 2014, respectively, and the Ph.D. degree in biomedical engineering from Erasmus University Medical Center, Rotterdam, The Netherlands, in 2019.

He is currently working as a Post-Doctoral Fellow with Erasmus University Medical Center. His research interests include high-frame-rate ultrasound imaging, blood-flow quantification, and ultrasound contrast agents.

Djalma Simoes dos Santos (Member, IEEE) received the M.Sc. degree in biomedical engineering from the University of São Paulo, São Paulo, Brazil, in 2018, and the Ph.D. degree in applied sciences from Delft University of Technology, Delft, The Netherlands, in 2024.

He is currently working as a Post-Doctoral Fellow at Delft University of Technology. His research interests include the design, modeling, fabrication, and characterization of ultrasound transducers for medical applications.

Emile Noothout received the bachelor's degree from the Intermediate Technical School for Mechanics, Dordrecht, The Netherlands, in 2004.

From 2004 to 2006, he was with the Leidse Instrumentmaker School, Leiden, The Netherlands, where he studied for Research Instrument Maker. From 2007 to 2013, he was a Research Instrument Maker with TNO, Delft, The Netherlands. Since 2013, he has been with Delft University of Technology, Delft, where he is involved in the development of medical ultrasound transducers and research assistance.

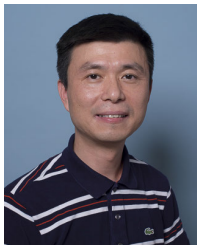

Zu-Yao Chang received the M.Sc. degree in electrical engineering from Delft University of Technology, Delft, The Netherlands, in 2003.

Since 2003, he has been a Staff Member with the Electronic Instrumentation Laboratory, Delft University of Technology, focusing on impedance measurement systems and smart sensor systems.

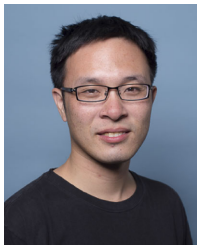

Chao Chen (Member, IEEE) received the B.Sc. degree in micro-electronics from Tsinghua University, Beijing, China, in 2010, and the M.Sc. (cum laude) and Ph.D. degrees in micro-electronics from Delft University of Technology, Delft, The Netherlands, in 2012 and 2018, respectively.

From 2017 to 2022, he was a Senior/Principal Analog IC Designer with Butterfly Network, Inc., Guilford, CT, USA. From 2021 to 2022, he was with Delft University of Technology, as a Post-Doctoral Researcher. In 2023, he founded Sonosilicon, a start-up that operates in both Hangzhou, China, and Delft, where he is currently the Chief Executive Officer. His research interests include integrated circuits for medical ultrasound and data converters.

Dr. Chen is a member of the Technical Program Committee of European Solid-State Electronics Research Conference (ESSERC). He was a recipient of the 2017 IEEE IUS Best Student Paper Award and the 2019 Else Kooi Award. He was a co-recipient of the 2021 ISSCC Anantha P. Chandrakasan Distinguished-Technical-Paper Award and Demonstration Award, the 2020 ISSCC Technology Innovation Award, and the 2017 A-SSCC Best Student Paper Award.

Vincent A. Henneken received the M.Sc. and Ph.D. degrees in mechanical engineering from Delft University of Technology, Delft, The Netherlands, in 2002 and 2008, respectively.

He has been working as a System Architect and the Project Leader in the field of micro-integration and MEMS ultrasound development for healthcare applications at Philips, Eindhoven, The Netherlands, since 2010. His main involvements are in developing technology solutions for the integration of ultrasound transducers with electronic functionality in medical devices, such as catheters and patches, aiming to improve medical procedures. He has been a Technical Project Leader in the ENIAC JU INCITE project and the ECSEL JU InForMed, POSITION-II, and Moore4Medical projects.

Nico de Jong (Member, IEEE) received the degree from Delft University of Technology, Delft, The Netherlands, in 1978, and the M.Sc. degree in applied physics in the field of pattern recognition and the Ph.D. degree in 1993, with a focus on acoustic properties of ultrasound contrast agents.

He has been the Vice Head of Biomedical Engineering with the Thoraxcenter, Erasmus University Medical Center, Rotterdam, The Netherlands, headed by Prof. Ton van der Steen. He has been the Head of the Medical Imaging Group, Delft University of Technology, until 2021. From 2003 to 2011, he was a part-time Professor with the University of Twente, Enschede, The Netherlands, in the Physics of Fluids Group headed by Prof. Detlef Lohse. He is the Founder and a Co-Organizer of the annual European Symposium (this year for the 28th time, see https://www.echocontrast.nl) on ultrasound contrast imaging, held in Rotterdam and attended by approximately 175 scientists from universities and industries all over the world. Currently, he has partly retired and still doing research at Delft University of Technology and the Erasmus University Medical Center. He has graduated 51 Ph.D. students and is currently supervising seven Ph.D. students.

Dr. de Jong has been an Associate Editor of Ultrasound in Medicine and Biology and has been the Guest Editor for special issues of several journals.

Hendrik J. Vos (Member, IEEE) received the M.Sc. degree in applied physics from Delft University of Technology, Delft, The Netherlands, and the Ph.D. degree from the Department of Biomedical Engineering, Erasmus University Medical Center, Rotterdam, The Netherlands, in 2004 and 2010, respectively.

He was a Postmaster Researcher with the University of Florence, Florence, Italy, and a Contract Researcher for the petrochemical industry on cutting-edge ultrasonic solutions. He currently is an Associate Professor with Erasmus University Medical Center and Delft University of Technology, Delft. He received a Dutch NWO-TTW-VIDI personal grant in 2018. His research interests include acoustical array technology for biomedical imaging in all its aspects: transducers, 2-D and 3-D beamforming, cardiac shear waves, ultrafast Doppler, contrast imaging, and related subclinical and clinical studies.

Johan G. Bosch (Member, IEEE) received the M.Sc. degree in electrical engineering from Eindhoven University of Technology, Eindhoven, The Netherlands, in 1985, and the Ph.D. degree from Leiden University, Leiden, The Netherlands, in 2006.

He is currently an Associate Professor with the Department of Biomedical Engineering, Thoraxcenter, Erasmus University Medical Center, Rotterdam, The Netherlands. He is a (Co-)Principal Investigator of projects on 3-D ultrasound image formation, transducer development, 2-D and 3-D cardiovascular imaging, and flow and tissue stiffness assessment using novel ultrasound approaches. His research interests include echocardiographic image processing, transducer development, and novel ultrasound techniques for image formation and functional imaging.

Martin D. Verweij (Member, IEEE) received the M.Sc. (cum laude) and Ph.D. degrees in electrical engineering from Delft University of Technology, Delft, The Netherlands, in 1988 and 1992, respectively.

In 1998, he became an Associate Professor with the Laboratory of Electromagnetic Research, Delft University of Technology, where he joined the Laboratory of Acoustical Wavefield Imaging in 2011. Since 2021, he has been heading the Ultrasound Group, Department of Imaging Physics, Delft University of Technology. His current research interests include dedicated transducer designs, beamforming algorithms, and theoretical modeling and numerical simulation of medical ultrasounds.

Michiel A. P. Pertijs (Senior Member, IEEE) received the M.Sc. and Ph.D. degrees (cum laude) in electrical engineering from Delft University of Technology, Delft, The Netherlands, in 2000 and 2005, respectively.

From 2005 to 2008, he was with National Semiconductor, Delft, where he designed precision operational amplifiers and instrumentation amplifiers. From 2008 to 2009, he was a Senior Researcher with Holst Centre, Eindhoven, The Netherlands. In 2009, he joined the Electronic Instrumentation Laboratory, Delft University of Technology, where he is currently an Associate Professor. He heads a research group focusing on integrated circuits for ultrasound applications. In 2023, he co-founded the company SonoSilicon, Delft, which specializes in chip technology for next-generation medical ultrasound devices. He has authored or co-authored two books, four book chapters, 15 patents, and more than 170 technical articles.

Dr. Pertijs is a member of the Technical Program Committees of European Solid-State Circuits Conference (ESSCIRC) and the IEEE International Ultrasonics Symposium (IUS). He served on the Program Committees of the International Solid-State Circuits Conference (ISSCC) and the IEEE Sensors Conference. He received the ISSCC 2005 Jack Kilby Award and the JSSC 2005 Best Paper Award. For his Ph.D. research on high-accuracy CMOS smart temperature sensors, he received the 2006 Simon Stevin Gezel Award from the Dutch Technology Foundation STW. In 2014 and 2023, he was elected Best Teacher of the EE program at Delft University of Technology. He served as an Associate Editor (AE) for IEEE OPEN JOURNAL OF SOLID-STATE CIRCUITS (O-JSSC) and IEEE JOURNAL OF SOLID-STATE CIRCUITS (JSSC).